Journal of Alloys and Compounds 935 (2023) 168211

Contents lists available at ScienceDirect

Journal of Alloys and Compounds

journal homepage: www.elsevier.com/locate/jalcom

Novel heterojunction superstrate Cu_2ZnInS_{4-x} (CZIS) thin film kesterite solar cell with vertical arrays of hexagonal ZnO nanorods window layer

Sodiq Tolulope Yussuf *, Morongwa Emmanuel Ramoroka, Siyabonga Beizel Mdluli, Kelechi Chiemezie Nwambaekwe, Precious Idinma Ekwere, Onyinyechi Vivian Uhuo, Chinwe Oluchi Ikpo, Emmanuel Iheanyichukwu Iwuoha *

Key Laboratory for NanoElectrochemistry, University of the Western Cape, 4th Floor Chemical Sciences Building, Robert Sobukwe Road, Bellville 7535, Cape Town, South Africa

ARTICLE INFO

Article history:
Received 1 August 2022
Received in revised form 2 November 2022
Accepted 23 November 2022
Available online 24 November 2022

Keywords:
Kesterite
Nanomaterials
Sol-gel synthesis
Thin film solar cells

ABSTRACT

Quaternary Cu_2ZnInS_{4-x} (CZIS) thin films have been prepared by a facile and cheap sol-gel spin coating technique. Low-temperature solution-based methods were used to fabricate a heterojunction solar cell in the superstrate architecture with CZIS thin film as the absorber, vertically aligned ZnO nanorod arrays, and CdS as the window and buffer layers respectively. ZnO nanorod arrays were prepared by hydrothermal technique and nanocrystal layer deposition technique were employed for the deposition of CdS-coated ZnO nanorod arrays. CZIS absorber layer was spin coated on the CdS-coated ZnO nanorod arrays and annealed at different temperatures. The vertically aligned ZnO nanorod arrays, and uniformly distributed CdS shell layer were confirmed from morphological studies. The device had a final configuration of Glass/ITO/ZnO NRs/CdS/CZIS/Ag. HRSEM revealed a nanoflake-like morphology and a band gap between 1.5 and 1.77 eV for the CZIS thin films. CZIS superstrate solar cell had a power conversion efficiency of ~ 0.61%, an open circuit voltage of ~ 0.8 V, a short circuit current of ~ 0.95 mA cm^{-2} and a fill factor of ~ 61.35%. This method demonstrates a novel, facile and eco-friendly technique for synthesizing nanocrystalline CZIS thin films with promising photo response from the fabricated device indicating a proof of principle that this material can find application in solar cells.

1. Introduction

Due to increase in the world's population and the relentless energy demand and consumption, the fabrication of inexpensive, environmentally friendly, and photovoltaic devices with high efficiency have received considerable attention from the photovoltaic research community for developing clean, and sustainable energy technologies. Among the various types of photovoltaic devices that have been studied in recent years, inorganic chalcogenide semiconductor materials when compared to silicon have tunable direct bandgaps and a high absorption coefficient that allows the conversion of 90% of the incident sunlight into electrical energy within a layer of few micrometers [1,2]. CdTe and CIGS are among the most successful inorganic thin film solar cells, with efficiencies of over 20%. However, they are hampered by the fact that the method involved in the production is highly expensive thereby hindering their scalability [3–7]. In the last decades, studies have shown that Cu_2ZnSnS_4 (CZTS) and its alloy $Cu_2ZnSn(S_xSe_{1-x})_4$ are low cost potential replacement/substituent to CdTe /CIGS based thin films solar cell. The reason being that their constituent elements are readily available, non-toxic, exhibit p-type conductivity, and have strong optical absorption of greater than 10^4 cm^{-1} in the electromagnetic spectrum visible region. In addition to the above, they have tunable direct bandgaps of 1.1–1.5 eV and high theoretical efficiency (32%) suitable for photovoltaic applications [7–13]. Ito and Nakazawa [14] were the first to fabricate a CZTS heterojunction diode by vacuum sputtering method. Several other researchers have fabricated CZTS/CZTSSe thin films by numerous methods such as sol gel spin coating, microwave, hot injection, electrodeposition, hydrothermal, spray pyrolysis, pulsed laser ablation, ultrasonic spray pyrolysis, thermal evaporation and sputtering [4,14–22]. Due to several benefits including low-temperature processing, decreased energy usage, simplicity of controlling the doping, stoichiometry, and deposition conditions, the sol-gel technique has been employed extensively among the aforementioned methods. Additionally, it is a low-cost method that is ideal for

* Corresponding authors.
E-mail addresses: 3773164@myuwc.ac.za (S.T. Yussuf), eiwuoha@uwc.ac.za (E.I. Iwuoha).

https://doi.org/10.1016/j.jallcom.2022.168211
0925-8388/

large-scale applications and emits less pollutants [23,24]. Despite reasonable research progress made on CZTS/CZTSSe the highest efficiency is still stalled at < 13%. It is a general consensus among kesterite researchers that the major factors causing the underperformance is the large open-circuit current voltage deficit, V_{OC} (600 meV) with respect to the theoretical maximum (i.e. the band gap, E_g, divided by the electron charge) which is much larger than 400 meV of CIGS-based solar cells [25]. Thus, the search for sustainable and affordable energy generation materials is still ongoing and a possible proposed approach to address the issue without having to sacrifice energy conversion efficiency is by partially substituting In with Zn [26]. In 2016, Ghosh et al. [26] developed a novel family of quaternary semiconductor Cu_2ZnAS_{4-x} and $CuZn_2AS_4$ (A = Al, Ga, In) nanocrystals and they were able to demonstrate that their novel nanomaterials possess the prerequisite optical properties for a material to be used as a cost effective and non-toxic absorber layers in photovoltaic applications. There is therefore no doubt that more novel materials will soon be developed as preparation technology is being continuously improved.

Majority of CZTS photovoltaic devices are fabricated with the architecture of Mo/CZTS/buffer/metal oxide nanostructures/metal electrodes and it has been shown that these configurations has some shortcomings such as metal oxide deterioration due to the thermal instability of the absorber layer which leads to the creation of the buffer interfaces and additionally, during heat treatment, there is usually an erosion reaction between CZTS and Mo back contact, as well as surface instability of CZTS. To address the aforementioned issues, one possible solution is to incorporate a superstrate structure in the solar cell, in which the metal oxide is directly deposited on the substrate preceded by annealing at a high temperature to prevent direct contact between CZTS and the conducting substrate [27]. The superstrate configuration is crucial for stability because a natural encapsulation and shielding of the window layer from the outside environment is provided by light entering the cell from the substrate side [28]. Combining the advantages of nanostructures with a thin film has been shown to improve the performance of thin film solar cells [2] and metal oxide nanostructures due to their controllable dimensions and aligned morphologies have been shown to provide a more effective charge generation, collection, and transfer due to the large junction area and the short collection distance to the interface. Several metal oxide nanostructures such as SnO_2, TiO_2, and ZnO have been widely used as photoanodes in quantum dots or dye-sensitized solar cells and bulk heterojunction solar cells [29]. Zinc oxide (ZnO), due to its large family of nanostructures is the most widely used and the most appropriate candidate for window layers in a superstrate solar cell because of its large optical band gap (3.30 eV), large exciton binding energy (60 meV) at room temperature and cheap cost [28,30]. In comparison to traditional spherical particles, vertically aligned ZnO nanorods enhances trapping of light in solar cells by increasing the diffuse reflection in between the nanorods thereby facilitating the separation of photogenerated charge carriers by facilitating charge transport along the axis of the nanorods which effectively reduces the recombination loss that originates from the particle-boundary electron hopping or scattering [28,31]. There are only a few studies in the literature on heterojunction superstrate solar cells employing metal oxide nanostructures. In 2012, Chen et al. [32] developed a solar cell with superstrate architecture of FTO/TiO_2/In_2S_3/CZTS/carbon entirely by a non-vacuum process and the solar cell had a short-circuit current density, open circuit voltage, fill factor and photovoltaic efficiency of 8.76 mA cm^{-2}, 250 mV, 0.27% and 0.6% respectively. Lee and Yong [29] prepared solution-based Cu_2ZnSnS_4 superstrate solar cell with the configuration CZTS/CdS/ZnO NR by using a vertically aligned ZnO nanorods and the device exhibited a maximum power conversion efficiency of 1.2% and a fill factor of 0.438. Berruet et al. [18] have achieved an efficiency of 3.53% using electrodeposition technique for a CZTS superstrate solar cell with the architecture of FTO/ TiO_2/In_2S_3/Cu_2ZnSnS_4/graphite. Ghosh et al. [2] combined hydrothermal, chemical bath deposition and spin coating assisted route for a Cd free kesterite Cu_2ZnSnS_4 thin film superstrate solar cell with the configuration ITO/ZnONR/ZnS/CZTS/Au and achieved a maximum power conversion efficiency of 3.63%. This is the highest efficiency ever reported for a metal oxide nanostructured superstrate CZTS solar cell.

In the present study, we have fabricated polycrystalline Cu_2ZnInS_{4-x} (CSIZ) thin films for the first time by a facile and an inexpensive sol-gel spin coating method. The effects of annealing temperature on the crystal structure, surface morphology and optical properties were also investigated. The window, buffer and absorber layer were all deposited by low temperature solution-based technique and a superstrate solar cell device was fabricated based on CZIS/CdS heterojunction with vertically aligned zinc oxide nanorod arrays. Sulfurization and selenization processes were avoided to prevent the oxidation and diffusion of CdS and the degradation of the ITO that may arise during the device fabrication processes.

2. Experimental details

2.1. Materials

Acetone (C_3H_6O, 99.8%), copper (II) chloride dihydrate ($CuCl_2$, ≥ 99.99% trace metal basis), ethanol (C_2H_5OH, 99.8%), hexamethylenetetramine (HMT) ($(CH_2)_6N_4$, ACS reagent ≥ 99.0%), indium (III) chloride ($InCl_3$, 98%), isopropanol ($CH_3CHOHCH_3$, 99.5%), 2-methoxyethanol ($CH_3OCH_2CH_2OH$, anhydrous, 99.8%), monoethanolamine ($HOCH_2CH_2NH_2$, purified by redistillation, ≥ 99.5%), thiourea (CH_4N_2S, ≥ 99%), zinc acetate dihydrate ($Zn(NO_3)_2.6\ H_2O$, 98%), zinc chloride ($ZnCl_2$, 98%), zinc nitrate hexahydrate ($Zn(NO3)_2{\cdot}6\ H_2O$) were purchased from Merck, Johannesburg, South Africa. The chemicals and solvents were used exactly as received with no further purification.

2.2. Preparation of vertically aligned ZnO nanorod (NR) arrays

Vertically aligned ZnO nanorod arrays was grown on a patterned indium tin oxide (ITO) coated glass substrates of sheet resistivity of 20 Ω/sq and size of 20 mm × 15 mm by hydrothermal synthetic route. Prior to the hydrothermal deposition, the patterned ITO glass substrate was cleaned ultrasonically in succession with 2% Hellmanex solution, acetone, ethanol, and isopropanol for 20 min each. Finally, the ITO coated substrates were dried by blowing with nitrogen. ZnO seed layer was synthesized from zinc acetate dihydrate, 2-methoxyethanol (solvent) and monoethanolamine (stabilizer). The method of Ghosh et al.[2] was used for the growth of ZnO nanorods with little modification. Firstly 0.5 M zinc acetate dihydrate was dissolved in a mixture of 0.5 M monoethanolamine and 2-methoxyethanol. Then, the resulting mixture was stirred at 60 º C for 2 h until a clear and transparent homogeneous solution was formed. Finally, the solution was aged for 24 h at room temperature. Afterwards 100 µL of the solution was spin coated on the ITO substrate at 3000 rpm for 30 s using a spin coater. The as deposited thin film was heated on a hotplate at 200 ºC for 30 min to remove the solvent. To increase the thickness, the spin coating and drying process were repeated three more times to achieve the desired thickness. After the formation of the seed layer, ZnO nanorod arrays were formed by suspending the ZnO seed layer upside-down in a 20 mL glass vial filled with an aqueous solution of 50 mM zinc nitrate hexahydrate and 50 mM hexamethylenetetramine (HMT) heated at 90 º C for 4 h and then rinsed with deionized water and ethanol for 1 min and blow dry with nitrogen then placed on a hotplate at 250 º C for 10 min.

2.3. Cadmium Sulphide (CdS) deposition on ZnO nanorod arrays

The nanocrystal layer deposition (NCLD) method was employed for the deposition of CdS on ZnO surfaces as reported by Lee and Yong [29]. The ZnO nanorods coated ITO substrates were immersed in a mixed aqueous precursor solution containing an equal amount of 20 mM $CdCl_2$ and 20 mM thioacetamide for 50 min at room temperature. After 50 min the samples were taken out and cleaned several times with distilled water and dried in air.

2.4. Photovoltaic device fabrication

To fabricate the heterojunction in a superstrate configuration, CZIS light absorber layer was coated on CdS-coated vertically aligned ZnO nanorod arrays by sol-gel spin coating technique. Ghosh et al.[2] with little modification was used for CZIS sol gel preparation. The sol gel was prepared by dissolving 0.4 M copper (II) chloride dihydrate, 0.2 M zinc chloride, 0.2 M indium (III) chloride and 2.4 M thiourea in 2-methoxyethanol and few drops of monoethanolamine was added as a stabilizer. To compensate for sulfur loss during the process of annealing, excess thiourea was used. The reagents were added in sequence and stirred at 50 °C for 1 h. A clear transparent sol-gel was obtained after one hour and it was spin coated on the CdS-ZnO nanorod arrays at 1500 rpm for 30 s and placed on a hot plate at 150 °C for 10 min to remove any unwanted solvent. After drying at 150 °C, it was transferred immediately to an already preheated hotplate at 250 °C and was annealed for 10 min. The spin coating, preheating and processes of annealing were repeated 3 times to achieve a thickness of between 800 nm and 1.00 µm. The solar cell devices were completed by carefully painting a silver paste across the ITO fingers and the top of the superstrate structure. After painting the Ag paste, the cell was placed on a hotplate at 100 °C to dry the paste. For CZIS thin films the annealing was done at 150, 250 and 350 °C respectively. Fig. 1 shows the schematic representation of fabricating the superstrate CZIS solar cell.

3. Characterization

X-ray Diffraction (XRD), Raman scattering, high-resolution scanning electron microscopy (HRSEM), energy dispersive X-ray spectroscopy (EDX) and UV–visible spectroscopy were used to characterize the thin films. The XRD patterns of CZIS, ZnO nanrods and CdS coated ZnO nanorods thin films were taken with a D8 Advance Multipurpose X-ray Diffractometer (BRUKER AXS, Berlin, Germany) with Cu-Kα radiation at a wavelength of 1.5406 Å fitted with a Lyn-Eye detector. The patterns of the XRD were collected from 15 to 70 (2θ) with a typical step size of 0.034 ° in 2θ and an effective time of 92 s per step. Raman spectra of the CZIS thin films were performed using Xplora Olympus BX41 Raman Spectrometer (Horiba, Tokyo, Japan) with a 532 nm laser as the excitation source. Optical absorption spectra of CZIS thin films, ZnO nanrods and CdS coated ZnO nanorods thin films were obtained using Varian Cary 300 UV-Vis-NIR spectrophotometer (Agilent, Santa Clara, CA, USA) in the wavelength region of 300 – 900 nm at room temperature. The morphological and elemental analyses of CZIS, ZnO nanrods and CdS coated ZnO nanorods thin films were performed with Auriga Field Emission Scanning Electron Microscope (FESEM) fitted with an Energy Dispersive X-ray Spectrophotometer (EDS) from Carl Zeiss Microscopy GmbH (Jena, Germany), which is operated at an acceleration of 200 kV. Current-voltage characterization of the heterojunction devices were measured with Ossila XTRALIEN X200 Source Measure Unit (Ossila Ltd, Sheffield, United Kingdom) using an illumination of AM 1.5 G, 100 mW cm^{-2} provided by a solar simulator (Sciencetech Inc., London, ON, Canada).

4. Results and discussion

The XRD pattern of the novel Cu_2ZnInS_{4-x} (CZIS) annealed at 150, 250 and 350 °C are presented in Fig. 2(a). To analyze the thin film for XRD, the precursor salts were spin coated on ITO substrate and annealed at different temperatures. All the films displayed peaks at 2θ equals 28.05 °, 32.85 °, 46.5 ° and 55.7 ° corresponding to (112), (200), (220) and (312) crystallographic planes of the kesterite crystal structure. At all the temperature studied the XRD pattern is consistent with the CZTS kesterite phase (JCPDS no-00–26–0575). This findings agrees well with similar reports on CZTS absorber [24]. The other observable peaks correspond to the ITO substrate. There are no observable peaks due to the precursor or impurity secondary phases. The substitution of Sn (0.69 Å) with In (0.80 Å) did not alter the tetragonal crystal structure arrangement although the peaks have shifted slightly to the left. This is because the ionic radius of In is higher than that of Sn so it therefore increases the lattice constant leading to a shift in the diffraction peak to a lower angle [33,34]. The average crystallite size is calculated from Scherrer formula relation [11,35].

$$D_{hkl} = k\lambda/\beta\cos\theta \tag{1}$$

where k is a constant (0.94), λ is the X-ray wavelength (Cu K-α = 1.5406 Å), β is the full width at half maximum (FWHM) of the diffraction peak (112), and θ is the position of the peak. The average crystallite size calculated from the most intense (112) peak of the XRD pattern at 150, 250 and 350 °C is about 15.0, 19.4 and 22.6 nm. Interplanar spacing and the lattice parameter of CZIS at different temperatures was calculated using Bragg's equation for tetragonal lattice [11,35,36].

$$n\lambda = 2dsin\theta \tag{2}$$

$$\frac{1}{d_{hkl}^2} = \frac{h^2}{a^2} + \frac{k^2}{a^2} + \frac{l^2}{c^2} \tag{3}$$

n is the order of diffraction, λ is the incident x-ray's wavelength, d is the interplanar spacing, θ is the position of the peak, h,k,l are the miller indices and a, c are the lattice parameters. The interplanar spacing of the most intense peak (112) at 150, 250 and 350 °C were found to be 0.3178 nm, 0.3147 nm and 0.3162 nm respectively. The interplanar spacing increases and then decreases with an increase in temperature. The lattice parameters a were calculated to be 5.487, 5.540 and 5.484 Å at 150, 250 and 350 °C while the c values were estimated to be 11.090, 10.598 and 10.911 Å respectively. The obtained values agree well with what has been found in the literature for kesterite CZTS crystal structure [37–39].

Tetragonal distortion (deviation of $c/2a$ from 1) is an important parameter in tetragonal structures and it is vital for electronic properties of materials. $c/2a$ values obtained for CZIS nanocrystals at 150, 250 and 350 °C is 1.0024, 09562 and 0.9948. It decreases with an increase in temperature. The higher the temperature the more tetragonal structure CZIS assume. These values agree well with what has been reported for tetragonal CZTS crystal structure in the literature [37–39]. The number of dislocations in a unit volume of a crystalline material (dislocation density) is calculated from the Williamson and Smallman's relation [11,35].

$$\delta = \frac{1}{D^2} \tag{4}$$

The strain of the thin film can also be measured using the relation [11,35].

$$\varepsilon = \frac{\beta\cot\theta}{4} \tag{5}$$

where δ is the dislocation density, ε is the strain, D is the crystallite size, β is the FWHM of the most intense diffraction peak, θ is the corresponding Bragg's angle of the thin films. Table 1 shows the

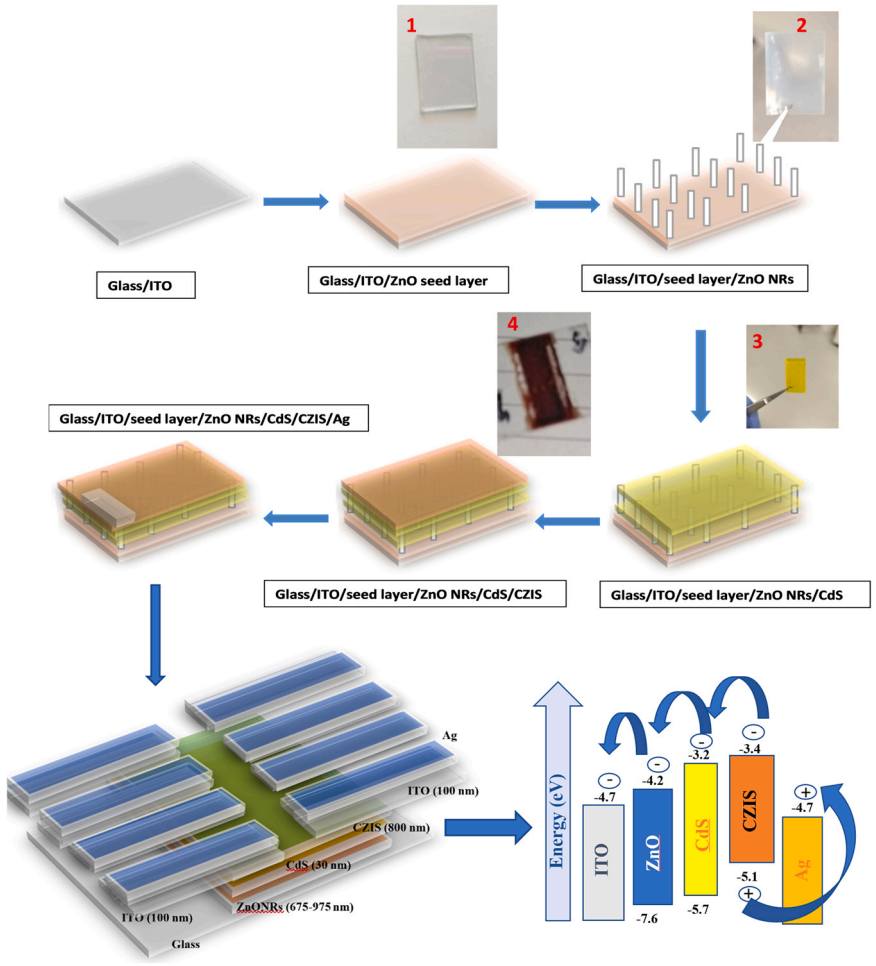

Fig. 1. Schematic representation of fabricating a superstrate CdS-coated ZnO nanorods copper zinc indium sulfide (CZIS) thin film solar cells and the completed solar structure. Inset - Photographs of (1) ZnO seed layer (2) ZnO NRs (3) CdS-coated ZnO NRs & (4) CZIS coated on CdS-coated ZnO NRs.

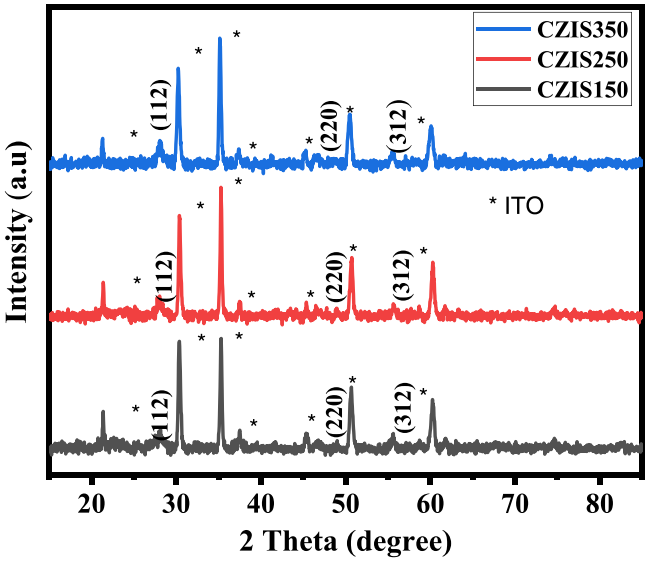

Fig. 2. (a) XRD patterns (b) Raman spectra of copper zinc indium sulfide at 150, 250 & 350 °C.

structural parameters of CZIS thin films at 150, 250 and 350 °C. One of the most significant unfavorable factors affecting structural properties that can result from geometric mismatch at the boundaries between crystalline lattices of films and substrates is stress. These stresses have the potential to cause microstrains (e) in the films. A crystal defect known as a dislocation occurs when the lattice in one area of the crystal is misregistered with that in another area. Crystallographic defects or dislocation disrupt the regular patterns [40]. The dislocation density and the microstrain in the CZIS thin films decreases with an increase in the annealing temperature indicating that as the temperature increases, there is a decrease in lattice imperfection and stress in the CZIS thin films resulting in the formation of a good crystalline structure at higher annealing temperature. The higher the crystallite sizes, the fewer the grain boundaries, the lower the dislocation density and microstrain [11,35].

Raman spectroscopy is a complimentary technique to XRD that is used to rule out the presence of secondary phases in the synthesized nanocrystalline materials or films. Fig. 3 shows the Raman spectra of CZIS thin films at 150, 250 and 350 °C. At 150 °C, CZIS thin film show most intense vibrational peaks at 340 cm^{-1}, broad peak at 280–320 cm^{-1} and a weak peak at 249 cm^{-1}, at 250 °C, CZIS thin film show most intense vibrational peaks at 340 cm^{-1}, a broad peak at 290–320 cm^{-1} and a weak peak at 260 cm^{-1} while at 350 °C, CZIS thin film show major vibrational peak at 337 cm^{-1}, a broad peak at 296 cm^{-1}, 320 cm^{-1} and a weak peak at 260 cm^{-1}. The peaks at 337–340 cm^{-1} corresponds to the pure anion mode of sulfur atom vibrations in CZTS kesterite lattice. The weak peaks at 245–260 cm^{-1} can also be assigned to CZTS [41–43]. The broad band at 280–320 cm^{-1} for 150 and 250 °C and the peaks at 296 cm^{-1}, 320 cm^{-1} for 350 °C could be attributed to tetragonal Cu-In-S phase

Table 1
Structural analysis of X-ray diffraction pattern for copper iron indium sulfide at 150, 250 and 350 °C.

Temp (°C)	Crystal structure	2θ	Lattice parameters (Å)		Unit Cell Volume V (Å)	Interplanar distance, d_{hkl} (Å)	Crystallite size, D_{hkl} (nm)	FWHM β (deg)	Dislocation density δ (10^{15} line m^{-2})	Strain ε
			$a = b$	c						
150	Kesterite	28.141	5.487	11.090	333.888	3.179	15.00	0.5530	4.440	0.5516
250	Kesterite	28.340	5.540	10.598	325.250	3.150	19.40	0.4267	2.660	0.4225
350	Kesterite	28.200	5.484	10.911	328.140	3.162	22.60	0.3663	1.960	0.3646

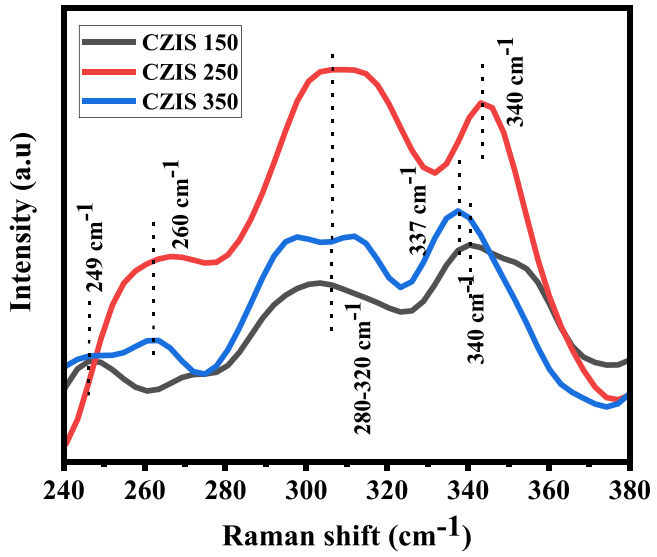

Fig. 3. Raman spectra of copper zinc indium sulfide at 150, 250 & 350 °C.

with a considerable copper deficiency [44]. This shows that in addition to the tetragonal CZTS kesterite phase, there also exist tetragonal Cu-In-S phase in our prepared thin films.

Fig. 4(a), (c) and (d) shows the HRSEM images of CZIS thin films annealed at various temperatures (150, 250 and 350 °C). At all temperatures the films are composed of a homogeneously distributed nanoflake like grains. The energy dispersive x-ray spectroscopy of the films as shown in Fig. 4(b), (d) and (f) confirms the presence of copper, zinc, indium, and sulfur. At 150 °C, the percentage atomic composition of Cu is 17.69%, Zn is 8.56%, In is 44.07% and S is 29.68%, at 250 °C, the percentage atomic composition of Cu is 18.6%, Zn is 8.53%, In is 47.06% and S is 25.82% while at 350 °C, Cu is 22.19%, Zn is 9.51%, In is 35.17% and S is 33.13%. All the thin films are slightly Cu rich, In rich and S poor. Irrespective of the annealing temperature used, the In concentration was more than that of Zn for all the CZIS thin films, which deviates from stoichiometry. This may be attributed to the chemical reactivity and different reaction rates of the chloride precursors in the solvents employed in the precursor solution [45,46].

The UV–visible absorbance spectra of CZIS at different temperature over the range of 350–1000 nm is presented in Fig. 5a. CZIS thin films show high absorption in the visible region showing their potential as photovoltaic absorber in solar cell applications. The absorbance increases with an increase in annealing temperature. The band gap of the CZIS films annealed at different temperatures were evaluated using Tauc's relation [28,47,48].

$$\alpha = \frac{A(h\nu - E_g)^n}{h\nu} \tag{6}$$

where E_g is the energy band gap, α is the absorption coefficient, A is a constant, and $h\nu$ is the incident photon energy, and n is the probability of transition, which depends on whether the optical transition is direct or indirect. The value of n is 0.5 for direct band gap semiconductor materials with allowed direct transition. The optical band gap can be calculated through the extrapolation of the linear part of the plot of $(\alpha h\upsilon)^2$ against $h\upsilon$ in the high absorption range and finding the intercept on the x-axis [28,47,48]. The optical band gap of CZIS thin films in Fig. 5b is the value of the intersection point with the x-axis and it was estimated to be 1.50, 1.65 and 1.77 eV respectively. There is an increase in the optical band gap with a decrease in the annealing temperature. The average grain size and the existence of numerous CZTS phases in the films are the two most important factors influencing the band gap of CZTS films. As a result, the decrease observed with an increase in annealing temperature in the optical bandgap of CZIS thin films may be ascribed to an increase in the average grain size and presence of secondary phase as confirmed by Raman spectroscopy analysis [49,50]. This value is comparable to what has been reported for Cu_2ZnInS_{4-x} using the hot injection method [26]. The obtained band gap values are comparable to what has been reported in the literature for CZTS and are suitable for solar cell applications [51–54].

The thin film's refractive index determines the possibility of total internal reflection within the solar cells [11]. The refractive index of CZIS thin films at different annealing temperature is calculated by the Moss relation [40].

$$E_g n^4 = k \tag{7}$$

where E_g is the band gap, n is the refractive index and k has a constant value of 108 eV [11,55]. The dielectric properties of a material refer to its ability to obstruct electron movement when polarized by an external electric field. To build effective solar cells, semiconducting materials with appropriate refractive index and dielectric constants are required since they are major determinant in the optical and electrical properties of the thin films [11,40]. The high-efficiency dielectric constant (ε_∞) of CZIS thin films was determined by the relation [40].

$$\varepsilon_\infty = n^2 \tag{8}$$

The static dielectric constant ε_o for the CZIS thin films is calculated using the equation [40].

$$\varepsilon_o = 18.52 - 3.08E_g \tag{9}$$

The band gap, refractive index and dielectric constant parameters of CZIS thin films annealed at 150, 250 and 350 °C are shown in Table 2. The obtained values are closely related to what has been reported for CZTS in the literature indicating that CZIS thin films have the appropriate optical properties required for the development of efficient solar cells [11,40].

The morphological features of ZnO nanorods were characterized by high resolution scanning electron microscopy as shown in Fig. 6. It can clearly be seen from the cross-sectional area of the HRSEM images that the ZnO nanorods aligned well and grow vertically on the ITO substrate. Image J software was used to calculate the distribution of the diameter and the length of the nanorods, and it was found to be in the range of 70–140 nm and 675–975 nm respectively.

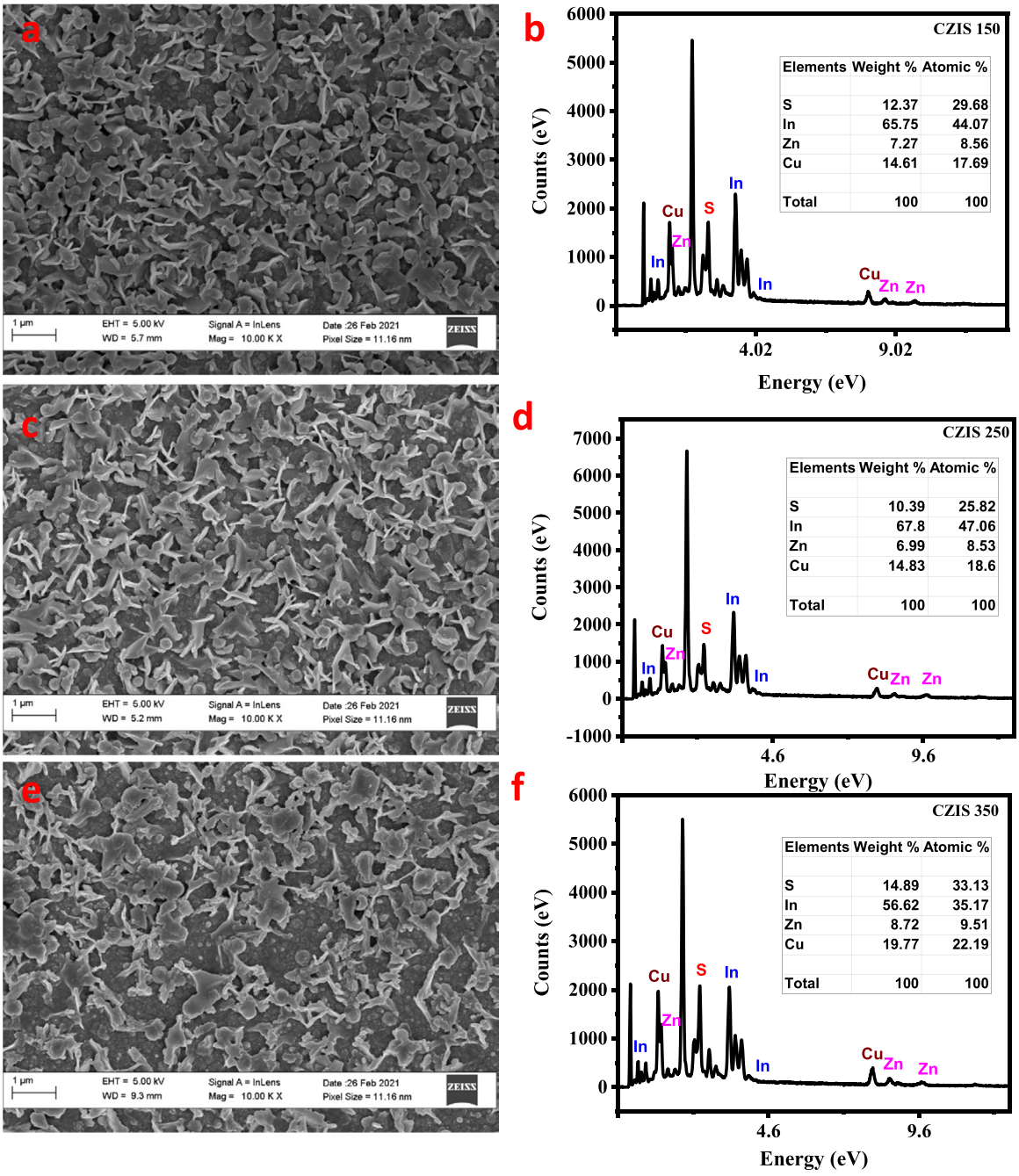

Fig. 4. SEM images and EDS plot of CZIS thin films 150, 250 & 350 °C.

The thickness of the nanorods as calculated from the cross-sectional area using imageJ software is approximately 1.10 µm. From the top view it can be seen that the ZnO thin film reveals hexagonal structure of the top of the nanorods. It can be observed that when CdS was deposited by nanocrystal layer deposition (NCLD) for 50 min, a uniform CdS shell layer was formed on the ZnO nanorods and the CdS layer covered the entire surface of the ZnO nanorod arrays. This method was used to deposit a uniform 30 nm CdS shell layer by Lee et al. [29]. The average elemental composition of the ZnO nanorods and CdS coated ZnO nanorods was determined by energy dispersive x-ray spectroscopy and displayed in Fig. 7(c) and (d). ZnO nanorod contains Zn and O in stoichiometric ratio of 1:1 and it also confirms that CdS-coated ZnO nanorods contains Zn, O, Cd and S. Morphological changes could be observed when CZIS was deposited by spin coating technique as shown in Fig. 6(e). It has been reported that a single coating of CZTS leads to an insufficient penetration that does not extend to the bottom of the ZnO nanorods thereby leading to films with defects such as cracks and voids which leads to reduction in the V_{OC} and *FF* values. In our case, a uniformly infiltrated film without visible cracks or voids was observed at two, three and four

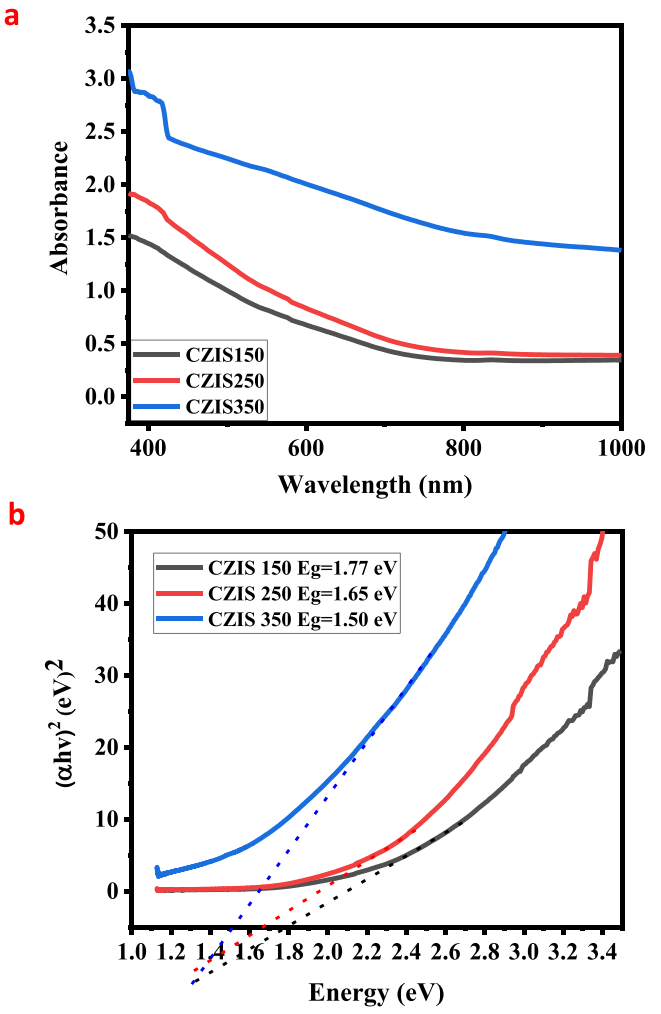

Fig. 5. (a) UV-Visible absorption spectra (b) experimental Tauc plots of CZIS thin films at 150, 250 & 350 °C.

coating cycles and the four coating cycles is shown in Figs. 5(e) and 7. Two coating cycles as reported by Lee et al. [29] gave the least efficiency for CZIS thin film solar cell devices studied at 150 °C.

The crystal structures of the ZnO nanorods were characterized using XRD studies and the XRD pattern is shown in Fig. 7(a) and (b). It shows a hexagonal wurtzite crystal structure for the ZnO nanorods showing a peak with a high intensity at 34.4 ° corresponding to the reflection from (002) crystallographic planes indicating that the nanorods preferred growth in the c-axis orientation [2,29]. Other weak peaks due to the reflection from (100), (010), (103) and (004) planes of the wurtzite ZnO (JCPDS card no. 4–0416) were also observed. The lattice parameter of the ZnO nanorods was calculated using Bragg's equation for hexagonal lattice and the lattice parameters were estimated to be a = 3.24 Å and c = 5.2 Å. This is consistent with the HRSEM results. After coating CdS on the ZnO nanorods by nanocrystal layer deposition, aside the ZnO nanorod peaks, other diffraction peaks were observed at 2θ equals 24.8 °, 26.5 °, 28.1 °, 43.6 °, 47.8 ° and 51.8 ° corresponding to (100), (002), (101), (110), (103) and (112) planes of

Table 2
The band gap, refractive index and dielectric constants of copper zinc indium sulphide thin films annealed at 150, 250 and 350 °C.

Temp (°C)	Band gap *Eg* (eV)	Refractive index *n*	High-frequency Dielectric constant ε_∞	Dielectric constant ε_o
150	1.77	2.795	7.811	13.068
250	1.65	2.844	8.090	13.438
350	1.50	2.913	8.486	13.900

hexagonal polycrystalline CdS (JCPDS-411049). From the XRD results it can be confirmed that the uniformly coated shell layer of CdS on the ZnO nanorods were structurally composed of polycrystalline CdS [29]. The UV–visible absorbance spectra of ZnO nanorods and CdS coated ZnO nanorods over the range of 350–100 nm is shown in Fig. 8(a). There is an increase in the absorbance in the visible region when CdS layer was coated on the ZnO nanorods. The absorbance peak at about 350 nm for ZnO nanorods were red shifted to about 500 nm for the CdS coated ZnO nanorods film. The shift in the absorbance peak in the visible region is because of quantum confinement of the very thin layer of CdS on the nanorods surface. The band gap of both the ZnO nanorods and the CdS coated ZnO nanorods were calculated using Tauc plot as shown in Fig. 8(b). The band gap of ZnO nanorods were found to be 3.24 eV while that of CdS coated ZnO nanorods showed two distinct extrapolated regions at 3.26 eV and 2.38 eV consistent with ZnO nanorods and CdS respectively. These values agrees well with what has been found in the literature [28,56]. The low band gap energy of CdS helps to improve light absorption in the visible region of the core/shell nanorods when coated on the ZnO nanorods [29].

The performance of CZIS superstrate solar cells was evaluated under AM 1.5 irradiation and the results are presented in Fig. 9. The device had a final configuration of Glass/ITO/ZnO NRs/CdS/CZIS/Ag and Glass/ITO/ZnO NRs/CZIS/Ag (Fig. 1). 8-pixel patterned ITO glass substrates were used for the fabrication. All the 8 cells made on the 8-pixel patterned ITO substrate had an effective area of 0.0256 cm^2. At first, CZIS solar cells with different thicknesses were fabricated at 150 °C by varying the number of spin coating times. CZIS sol gel were spin coated two, three and four times respectively. Fig. 6(e) shows that the thickness of CZIS with four coatings is about 800 nm as measured by image J which implies that a coating is about 200 nm. The solar cell with the four coatings had the best efficiency of 0.6092%, an open circuit voltage (*Voc*) of 0.8056 V, a short circuit current density (*Jsc*) of 0.9534 mA cm^{-2} and a fill factor (*FF*) of 61.35%. The photovoltaic parameters of all the solar cell devices are summarized in Table 3. The efficiency increases with an increase in CZIS absorber thickness. The reason for the low efficiency observed with the absorber layer with two coatings may be because it is too thin to absorb sufficient light to generate enough light-induced charges thereby resulting in low photocurrent generation [57]. Solar cell devices were then made with the absorber with the highest thickness at different annealing temperatures with and without CdS buffer layer. The power conversion efficiency of the devices made without CdS layer increased from 0.4405% to 0.6958% with an increase in the annealing temperature while the power conversion efficiency of the devices made with CdS buffer layer decreased from 0.6092% to 0.2973% with an increase in the annealing temperature from 150 to 350 °C. The champion of the solar cells made without CdS buffer layer had an efficiency of 0.6956%, a *Voc* of 1.6282 V, a *Jsc*

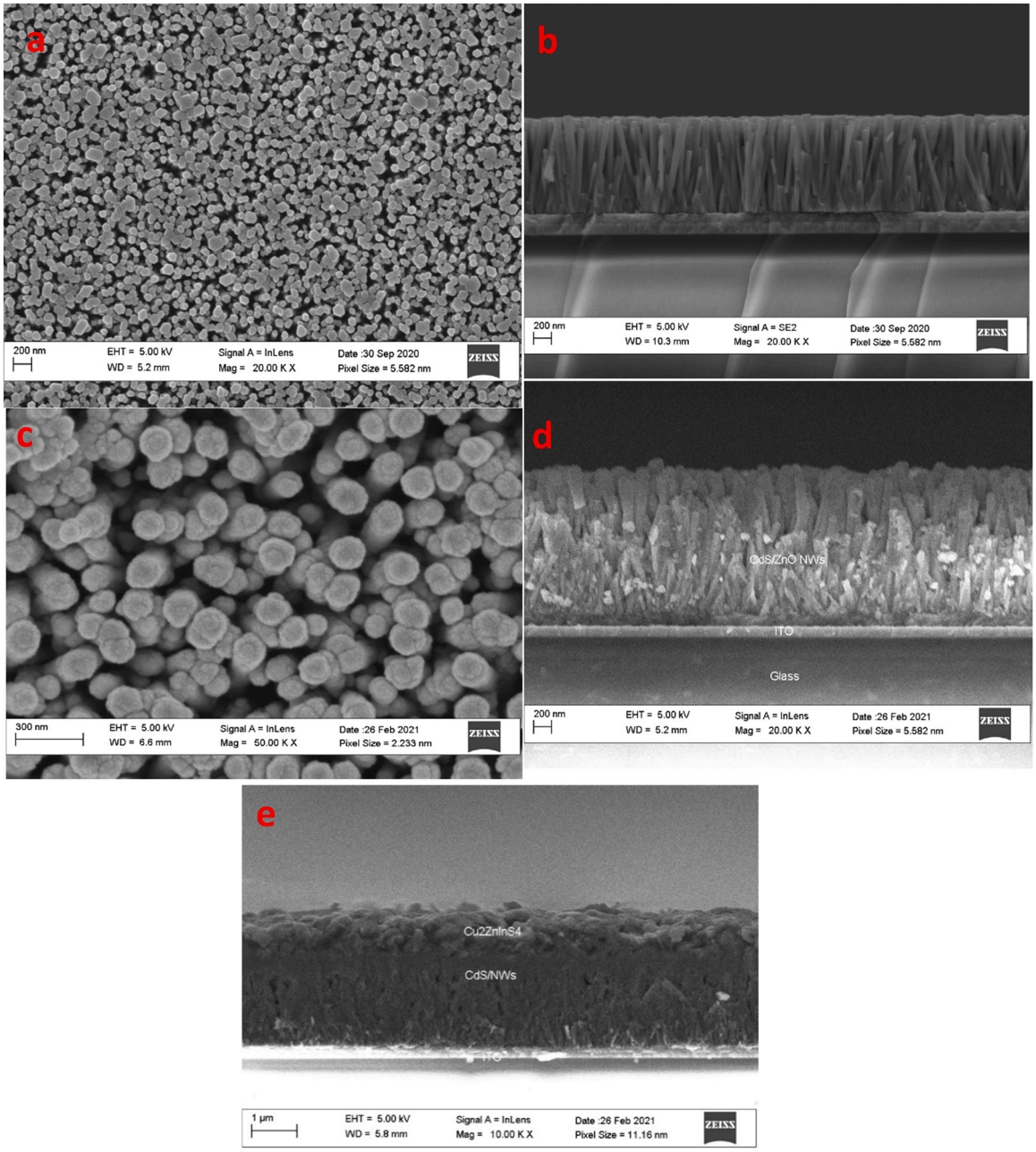

Fig. 6. Top view and cross-sectional HRSEM images of (a), (b) ZnO NRs, (c), (d) CdS-coated ZnO NRs (e) CIZS spin coated 4 times on CdS-coated ZnO NRs.

of 0.9327 mA cm^{-2} and an *FF* of 45.80% at 350 °C while the best device was made at 150 °C with CdS buffer layer having an efficiency of 0.6092%, a *Voc* of 0.8056 V, a *Jsc* of 0.9534 mA cm^{-2} and an *FF* of 61.35%. The increase in the efficiencies with an increase in the annealing temperature observed for the solar cell devices made without CdS buffer layer is as a result of an improvement in the crystallinity of the CZIS/ZnO NRs interface with an increase in the temperature while the decrease observed with an increase in annealing temperature with the solar devices made with CdS buffer layer is due to the disruption of the CZIS/CdS interface as a result of the possible inter-diffusion of CdS at higher temperatures [29]. The reason for the low efficiency of our devices is because of the large series resistance caused by the poor quality of the flaky like crystals which has been shown to increase the grain boundaries invariably leading to an increase in the number of recombination centers and it also restrict the flow of charge carriers [58]. This leads to a drop in the V_{OC} and consequently leads to a drop in the *FF* resulting in a poor power conversion efficiency [28]. To the best of our knowledge, there have been no reports on any CZIS solar devices either in the substrate or superstrate configuration. We therefore compare our results to superstrate CZTS that employed vertically aligned nanorods without post sulfurization or selenization. Table 4 shows the

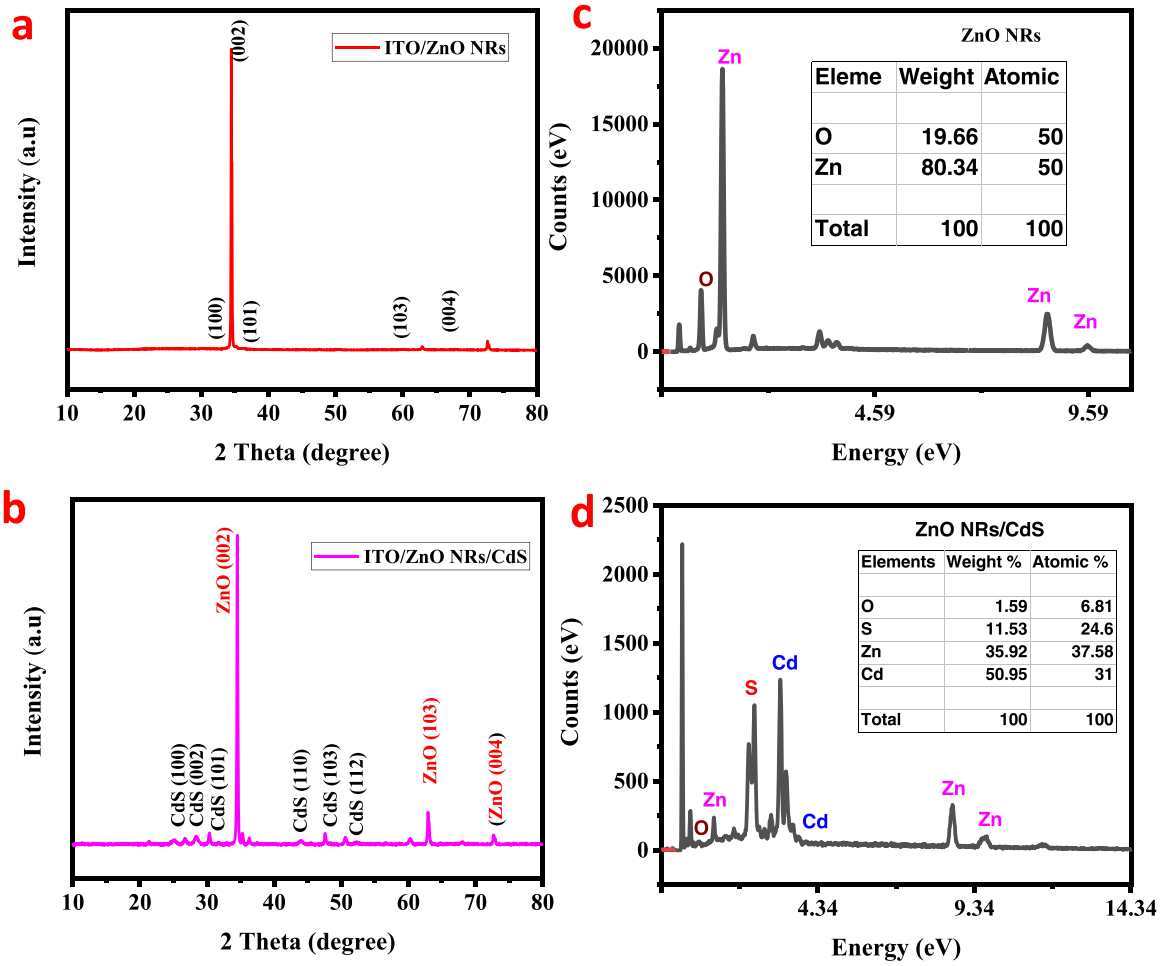

Fig. 7. XRD patterns of (a) ZnO NRs (b) CdS-coated ZnO NRs, EDS plot of (c) ZnO NRs (d) CdS-coated ZnO NRs.

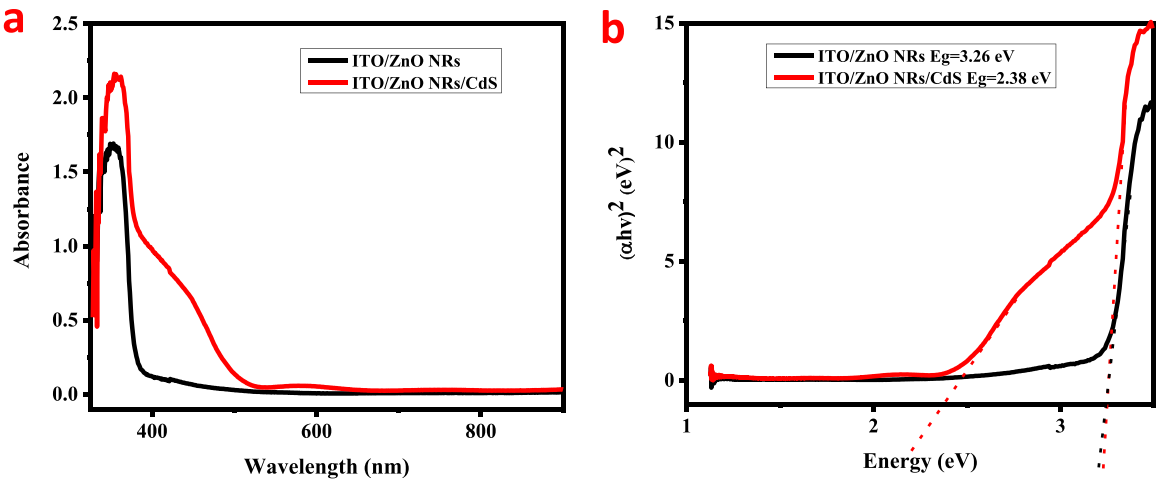

Fig. 8. UV-Visible absorption spectra of (a) ZnO NRs & CdS-coated ZnO NRs, (b) experimental Tauc plots of ZnO NRs & CdS-coated ZnO NRs.

comparison of this work to other similar superstrate CZTS solar cell devices found in the literature. When compared to results found in the literature for CZTS superstrate solar cells, it can be observed that the V_{OC} and the *FF* of the best CZIS superstrate devices is higher than most reported for CZTS found in the literature while the J_{SC} is higher than that reported by Varadharajaperumal et al. [59]. Even though the efficiency is low, it is better than the very first sulfide CNTS thin film solar cell (0.09%) [60], the very first pure sulfide CZTS device with 0.23% [61] and 0.08% obtained by Gayen et al. [28] for CZTS superstrate solar cell without employing ZnS buffer layer which is an

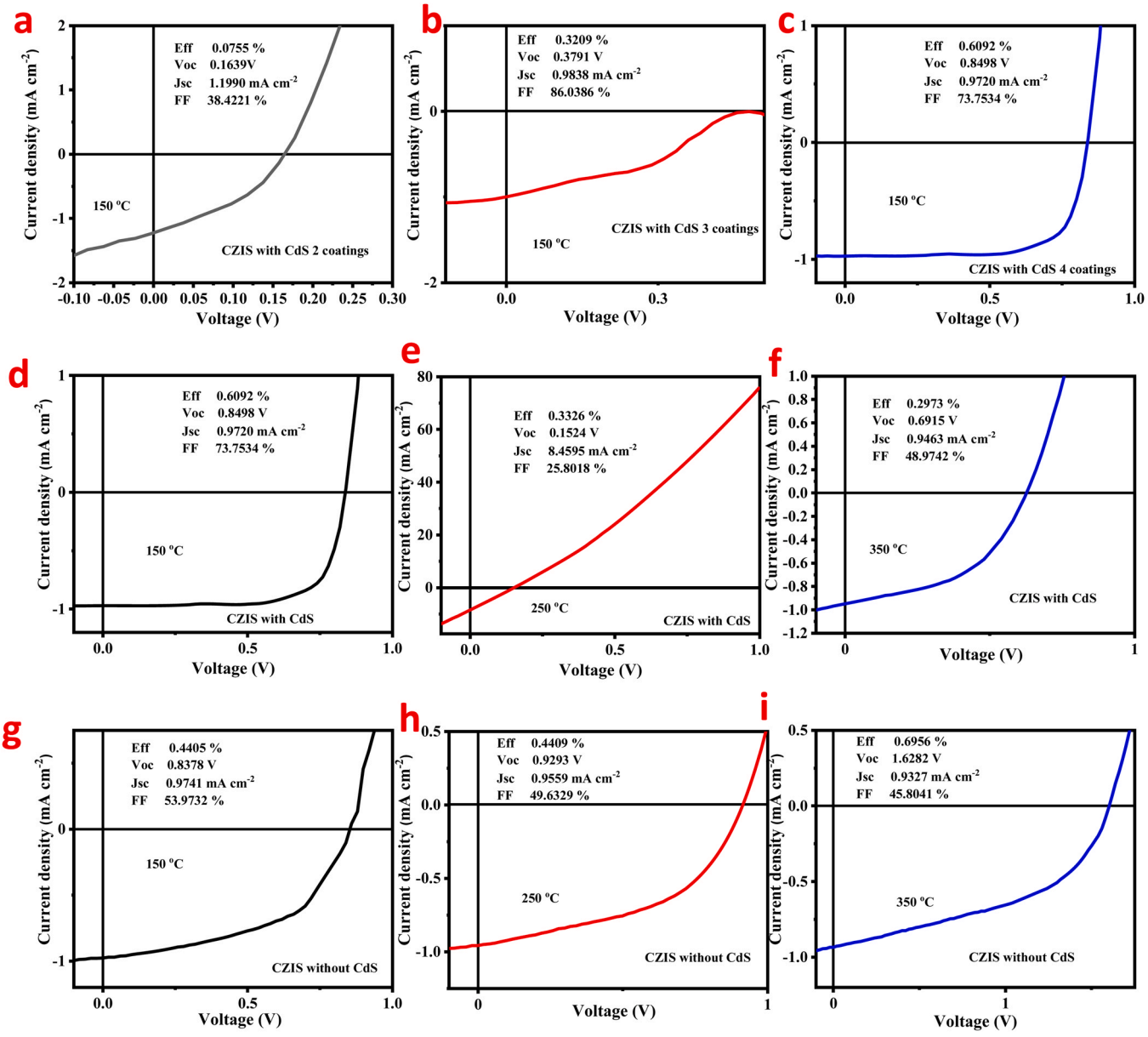

Fig. 9. I-V characteristics of Glass/ITO/ZnONRs/CdS/CIZS/Ag superstrate heterojunction solar cells under AM 1.5 G simulated illumination (100 mW cm^{-2}) (a) CZIS with 2 coatings (b) CZIS with 3 coatings (c) CZIS with 4 coatings at 150 °C (d) CZIS with CdS at 150 °C (e) CZIS with CdS at 250 °C (f) CZIS with CdS at 350 °C and Glass/ITO/ZnONRs/CIZS/Ag (g) CZIS without CdS at 150 °C (h) CZIS without CdS at 250 °C (i) CZIS without CdS at 350 °C.

Table 3
Photovoltaic parameters of CZIS superstrate heterojunction solar cells fabricated with and without CdS buffer layer.

Cell structure	*Eff* (%)	J_{SC} (mA cm^{-2})	V_{OC} (V)	*FF*	R_s (Ω cm)	R_{sh} (Ω cm)
ITO/ZnONRs/CdS/CIZS/Ag CZIS 150 °C - 2 coatings	0.0755	1.1990	0.1639	38.4211	50.1812	263.0142
ITO/ZnONRs/CdS/CIZS/Ag CZIS 150 °C - 3 coatings	0.3209	0.9838	0.3791	86.0386	400.1700	753.9808
ITO/ZnONRs/CdS/CIZS/Ag CZIS 150 °C - 4 coatings	0.6092	0.95343	0.8056	61.3478	36.7618	4982.3330
ITO/ZnONRs/CdS/CIZS/Ag CZIS 250 °C - 4 coatings	0.3326	8.4595	0.1524	25.8018	17.0188	18.7064
ITO/ZnONRs/CdS/CIZS/Ag CZIS 350 °C - 4 coatings	0.2973	0.9463	0.6415	48.9742	167.5693	1590.763
ITO/ZnONRs/CIZS/Ag CZIS 150 °C - 4 coatings	0.4405	0.9741	0.8378	53.9732	196.3007	5881.15
ITO/ZnONRs/CIZS/Ag CZIS 250 °C - 4 coatings	0.4409	0.9559	0.9293	49.6329	205.6896	2722.13
ITO/ZnONRs/CIZS/Ag CZIS 350 °C - 4 coatings	0.6956	0.9327	1.6282	45.8041	225.7040	3253.197

Table 4
Comparison of the present work to the literature that utilized ZnO nanorods and the most recent superstrate CZTS superstrate solar cells.

Device architecture	Deposition methods	V_{OC} (mV)	J_{SC} (mA cm^{-2})	*FF* (%)	*PCE* (%)	Ref
SLG/ITO/ZnO NRs/CdS/CZTS/Au	Precursor solution/Spin coating	679.2	4.100	43.8	1.20	[29]
Glass/ITO/ZnO NRs/ZnS/CZTS/Au	Sol-gel/Spin coating	868.9	8.500	49.1	3.63	[2]
Flexible substrate/FTO/ZnO NRs/CZTS/Carbon conductive adhesive tapes	Microwave/ Drop casting	405	4.350	46.9	0.83	[39]
Glass/FTO/ZnO NRs/ZnS/CZTS/Au	Sol-gel/Spin coating	454.0	5.652	41.6	1.07	[28]
Glass/FTO/ZnO NRs/ZnS/CZTS/Au	Sol-gel/Spin coating	285.0	0.837	35.9	0.08	
Glass/FTO/TiO_2/CdS/CZTS/Au	Molecular precursor solution/Spin coating	518	5.143	–	1.04	[62]
SLG/FTO/ZnO NWs/CdS/CZTS/Ag	Precursor solution deposition/Spin coating	589	7.070	54.0	2.27	[63]
Glass/ITO/ZnONRs/CdS/CZIS/Ag	Sol-gel/Spin coating	805.6	0.953	61.3	0.61	This work
Glass/ITO/ZnONRs/CZIS/Ag	Sol-gel/Spin coating	1628.2	0.933	45.8	0.70	

indication that optimizing the methods, the morphology, the composition and the processes involved in the fabrication of the device can further increase the efficiency of CZIS thin film solar cells.

5. Conclusion

In summary, polycrystalline CZIS thin films with kesterite crystal structure with nanoflake like morphology have been synthesized for the first time by a facile and an inexpensive sol-gel spin coating method without any post sulfurization processes. A superstrate solar cell with the configuration Glass/ITO/ZnONRs/CdS/CZIS/Ag and Glass/ITO/ZnONRs/CZIS/Ag were then fabricated using an all-solution process technique employing a CdS-coated ZnO nanorod arrays at different annealing temperatures. HRSEM studies confirmed the hexagonal shaped vertically aligned ZnO nanorod arrays and a homogeneously deposited CdS shell layer on the ZnO nanorod arrays and a crack free uniformly coated CZIS films which completely infiltrated the CdS-coated ZnO NR arrays. The champion device fabricated without CdS buffer layer had a maximum conversion efficiency of 0.6956%, a *Voc* of 1.6282 V, a *Jsc* of 0.9327 mA cm^{-2} and an *FF* of 45.80% at 350 °C while the best device was made at 150 °C with CdS buffer layer having an efficiency of 0.6092%, a *Voc* of 0.8056 V, a *Jsc* of 0.9534 mA cm^{-2} and an *FF* of 61.35% Considering that this is the first time of reporting this material as a solar cell absorber, it shows a promising prospect for solar cell applications.

CRediT authorship contribution statement

Sodiq Tolulope Yussuf: Conceptualization, Methodology, Writing – original draft. **Morongwa Emmanuel Ramoroka:** Methodology, Data curation. **Siyabonga Beizel Mdluli:** Methodology, Data curation. **Kelechi Chiemezie Nwambaekwe:** Software, Data curation. **Precious Idinma Ekwere:** Visualization**, Onyinyechi Vivian Uhuo:** Data curation, Validation. **Chinwe Oluchi Ikpo:** Validation, Editing. **Emmanuel Iheanyichukwu Iwuoha:** Conceptualization, Supervision, Writing – review & editing.

Data availability

The authors are unable or have chosen not to specify which data has been used.

Declaration of Competing Interest

The authors declare that they have no known competing financial interests or personal relationships that could have appeared to influence the work reported in this paper.

Acknowledgments

This work was funded by research grants awarded by the National Research Foundation (NRF) of South Africa: (i) the Blue Skies Research Programme Grant No.: 110981; and (ii) the South African Research Chair Initiative (SARChI) Grant No.: 85102.

References

[1] D. Aldakov, A. Lefrançois, P. Reiss, Ternary and quaternary metal chalcogenide nanocrystals: Synthesis, properties and applications, J. Mater. Chem. C. vol. 1, (24) (2013) 3756–3776, https://doi.org/10.1039/c3tc30273c
[2] A. Ghosh, R. Thangavel, A. Gupta, Solution-processed Cd free kesterite Cu_2ZnSnS_4 thin film solar cells with vertically aligned ZnO nanorod arrays, J. Alloy. Compd. vol. 694, (2017) 394–400, https://doi.org/10.1016/j.jallcom.2016.09.325
[3] T.D. Lee, A.U. Ebong, A review of thin film solar cell technologies and challenges, Renew. Sustain. Energy Rev. vol. 70, (September 2015) (2017) 1286–1297, https://doi.org/10.1016/j.rser.2016.12.028
[4] S. Engberg, J. Symonowicz, J. Schou, S. Canulescu, K.M.Ø. Jensen, Characterization of Cu2ZnSnS4 particles obtained by the hot-injection method, ACS Omega vol. 5, (18) (2020) 10501–10509, https://doi.org/10.1021/acsomega.0c00657
[5] J.H. Malik, M.B. Zaman, R. Poolla, K.A. Malik, I. Assadullah, A.A. Bhat, R. Tomar, Hydrothermal synthesis of tetragonal and wurtzite Cu_2MnSnS_4 nanostructures for multiple applications: Influence of different sulfur reactants on growth and properties, Mater. Sci. Semicond. Process. vol. 121, (2021) 105438, https://doi.org/10.1016/j.mssp.2020.105438
[6] S.P. Madhusudanan, M. Suresh Kumar, K. Mohanta, S.K. Batabyal, Photoactive Cu_2FeSnS_4 thin films: Influence of stabilizers, Appl. Surf. Sci. vol. 535, (2021) 147600, https://doi.org/10.1016/j.apsusc.2020.147600
[7] M. Jamil, M. Amami, A. Ali, K. Mahmood, N. Amin, Numerical modeling of AZTS as buffer layer in CZTS solar cells with back surface field for the improvement of cell performance, Sol. Energy vol. 231, (2022) 41–46, https://doi.org/10.1016/j.solener.2021.11.025
[8] L. Huang, J. Li, S. Wang, L. Zhong, X. Xiao, Forming an Ultrathin SnS Layer on Cu_2ZnSnS_4 Surface to Achieve Highly Efficient Solar Cells with Zn(O,S) Buffer, Sol. RRL vol. 4, (5) (2020) 2000010, https://doi.org/10.1002/solr.202000010
[9] B. Liu, J. Guo, R. Hao, L. Wang, K. Gu, S. Sun, A. Aierken, Effect of Na doping on the performance and the band alignment of CZTS/CdS thin film solar cell, Sol. Energy vol. 201, (2020) 219–226, https://doi.org/10.1016/j.solener.2020.02.088
[10] S. Enayati Maklavani, S. Mohammadnejad, Enhancing the open-circuit voltage and efficiency of CZTS thin-film solar cells via band-offset engineering, Opt. Quantum Electron. vol. 52, (2) (2020) 1–22, https://doi.org/10.1007/s11082-019-2180-6
[11] A. Sharmin, M.S. Bashar, M. Sultana, S.M.M. Al Mamun, Sputtered single-phase kesterite Cu_2ZnSnS_4 (CZTS) thin film for photovoltaic applications: Post annealing parameter optimization and property analysis, AIP Adv. vol. 10, (1) (2020) 015230, https://doi.org/10.1063/1.5129202

[12] M. Mirzaei, J. Hasanzadeh, A. Abdolahzadeh Ziabari, Significant Efficiency Enhancement in Ultrathin CZTS Solar Cells by Combining Al Plasmonic Nanostructures Array and Antireflective Coatings, Plasmonics vol. 1, (2021) 3, https://doi.org/10.1007/s11468-021-01379-9

[13] S.R. Rondiya, Y.A. Jadhav, A. Živković, S.B. Jathar, G.K. Rahane, R.W. Cross, A.V. Rokade, R.S. Devan, S. Kolekar, R.L.Z. Hoye, H.N. Ghosh, N.H. de Leeuw, S.R. Jadkar, N.Y. Dzade, Solution-processed Cd-substituted CZTS nanocrystals for sensitized liquid junction solar cells, J. Alloy. Compd. vol. 890, (2022), https://doi.org/10.1016/j.jallcom.2021.161575

[14] K. Ito, T. Nakazawa, Electrical and optical properties of stannite-type quaternary semiconductor thin films, Jpn. J. Appl. Phys. vol. 27, (11R) (1988) 2094–2097, https://doi.org/10.1143/JJAP.27.2094

[15] Z. Su, K. Sun, Z. Han, H. Cui, F. Liu, Y. Lai, J. Li, X. Hao, Y. Liu, M.A. Green, Fabrication of Cu_2ZnSnS_4 solar cells with 5.1% efficiency via thermal decomposition and reaction using a non-toxic sol-gel route, J. Mater. Chem. A vol. 2, (2) (2014) 500–509, https://doi.org/10.1039/c3ta13533k

[16] S.A. Vanalakar, G.L. Agwane, M.G. Gang, P.S. Patil, J.H. Kim, J.Y. Kim, A mild hydrothermal route to synthesis of CZTS nanoparticle inks for solar cell applications, Phys. Status Solidi vol. 12, (6) (2015) 500–503, https://doi.org/10.1002/pssc.201400261

[17] A.H. Pinto, S.W. Shin, E. Isaac, T.R. Knutson, E.S. Aydil, R.L. Penn, Controlling Cu_2ZnSnS_4 (CZTS) phase in microwave solvothermal synthesis, J. Mater. Chem. A vol. 5, (44) (2017) 23179–23189, https://doi.org/10.1039/c7ta06086f

[18] M. Berruet, Y. Di Iorio, C.J. Pereyra, R.E. Marotti, M. Vázquez, Highly-efficient superstrate Cu_2ZnSnS_4 solar cell fabricated low-cost methods, Phys. Status Solidi - Rapid Res. Lett. vol. 11, (8) (2017) 2–6, https://doi.org/10.1002/pssr.201700144

[19] S. Kala, H. Kaur, A. Rastogi, V.N. Singh, T.D. Senguttuvan, Structural and optoelectronic features of pulsed laser ablation grown Cu_2ZnSnS_4 films for photovoltaic applications, J. Alloy. Compd. vol. 658, (2016) 324–330, https://doi.org/10.1016/j.jallcom.2015.10.214

[20] X. Zeng, K.F. Tai, T. Zhang, C.W.J. Ho, X. Chen, A. Huan, T.C. Sum, L.H. Wong, $Cu_2ZnSn(S,Se)_4$ kesterite solar cell with 5.1% efficiency using spray pyrolysis of aqueous precursor solution followed by selenization, Sol. Energy Mater. Sol. Cells vol. 124, (2014) 55–60, https://doi.org/10.1016/j.solmat.2014.01.029

[21] V. Baskaran, S. Sakthivel, Current-voltage characteristics of Cu_2ZnSnS_4 absorber layer for energy harvesting devices, Mater. Res. Express vol. 6, (2019) 126333, https://doi.org/10.1088/2053-1591/ab6f34

[22] A.A. Ahmad, A.B. Migdadi, A.M. Alsaad, I.A. Qattan, Q.M. Al-Bataineh, A. Telfah, Computational and experimental characterizations of annealed Cu_2ZnSnS_4 thin films, Heliyon vol. 8, (1) (2022) e08683, https://doi.org/10.1016/j.heliyon.2021.e08683

[23] D.A. Elhaj, A.E. Kissani, M. Elyaagoubi, H.A. Dads, F. Welatta, L. Nkhaili, H. Chaib, A. Outzourhit, Development of Cu_2NiSnS_4 based thin film solar cells without a sulfurization step, Mater. Sci. Semicond. Process. vol. 107, (October 2019) (2020) 104811, https://doi.org/10.1016/j.mssp.2019.104811

[24] A. Tumbul, F. Aslan, A. Göktaş, I.H. Mutlu, All solution processed superstrate type Cu_2ZnSnS_4 (CZTS) thin film solar cell: Effect of absorber layer thickness, J. Alloy. Compd. vol. 781, (2019) 280–288, https://doi.org/10.1016/j.jallcom.2018.12.012

[25] A.H. Pinto, S.W. Shin, A. Sharma, R.L. Penn, E.S. Aydil, Synthesis of $Cu_2(Zn_{1-x}Co_x)SnS_4$ nanocrystals and formation of polycrystalline thin films from their aqueous dispersions, J. Mater. Chem. A vol. 6, (3) (2018) 999–1008, https://doi.org/10.1039/c7ta06295h

[26] A. Ghosh, S. Palchoudhury, R. Thangavel, Z. Zhou, N. Naghibolashrafi, K. Ramasamy, A. Gupta, A new family of wurtzite-phase Cu_2ZnAS_{4-x} and $CuZn_2AS_4$ (A = Al, Ga, In) nanocrystals for solar energy conversion applications, Chem. Commun. vol. 52, (2) (2016) 264–267, https://doi.org/10.1039/c5cc07743e

[27] R. Yan, L. Kang, Y. Sun, J. Zhang, Solution-processed Cu_2ZnSnS_4 thin film with mixed solvent and its application in superstrate structure solar cells, RSC Adv. vol. 8, (21) (2018) 11469–11477, https://doi.org/10.1039/c8ra01095a

[28] R.N. Gayen, T. Chakrabarti, Effect of series and shunt resistance on the photovoltaic properties of solution-processed zinc oxide nanowire based CZTS solar cell in superstrate configuration, Mater. Sci. Semicond. Process. vol. 100, (April) (2019) 1–7, https://doi.org/10.1016/j.mssp.2019.04.018

[29] D. Lee, K. Yong, Solution-processed Cu_2ZnSnS_4 superstrate solar cell using vertically aligned ZnO nanorods, Nanotechnology vol. 25, (6) (2014), https://doi.org/10.1088/0957-4484/25/6/065401

[30] Y. Guo, J. Wei, Y. Liu, T. Yang, Z. Xu, Surfactant-Tuned Phase Structure and Morphologies of Cu_2ZnSnS_4 Hierarchical Microstructures and Their Visible-Light Photocatalytic Activities, Nanoscale Res. Lett. vol. 12, (1) (2017), https://doi.org/10.1186/s11671-017-1868-4

[31] X. Liu, C. Wang, J. Xu, X. Liu, R. Zou, L. Ouyang, X. Xu, X. Chen, H. Xing, Fabrication of ZnO/CdS/Cu_2ZnSnS_4 p-n heterostructure nanorod arrays via a solution-based route, CrystEngComm vol. 15, (6) (2013) 1139–1145, https://doi.org/10.1039/c2ce26829a

[32] Q. Chen, S. Cheng, S. Zhuang, X. Dou, Cu_2ZnSnS_4 solar cell prepared entirely by non-vacuum processes, Thin Solid Films vol. 520, (19) (2012) 6256–6261, https://doi.org/10.1016/j.tsf.2012.05.074

[33] G.S.D. Babu, X.S. Shajan, A. George, P. Parameswaran, S. Murugesan, R. Divakar, E. Mohandas, S. Kumaresan, G.M. Rao, Low-cost hydrothermal synthesis and characterization of pentanary $Cu_2ZnxNi_{1-x}SnS_4$ nanoparticle inks for thin film solar cell applications, Mater. Sci. Semicond. Process. vol. 63, (2017) 127–136, https://doi.org/10.1016/j.mssp.2017.02.015

[34] A. Sarilmaz, F. Ozel, Synthesis of band-gap tunable earth-abundant CXTS (X= Mn +2, Co+2, Ni+2 and Zn+2) nanorods: Toward a generalized synthesis strategy of quaternary chalcogenides, J. Alloy. Compd. vol. 780, (2019) 518–522, https://doi.org/10.1016/j.jallcom.2018.11.370

[35] H. Hammami, M. Marzougui, H. Oueslati, M. Ben Rabeh, M. Kanzari, Synthesis, Growth and Characterization of Cu_2CoSnS_4 Thin Films via Thermal Evaporation Method, Opt. (Stuttg.) vol. 227, (2021) 166054, https://doi.org/10.1016/j.ijleo.2020.166054

[36] S.K. Dwivedi, S.K. Tripathi, D.C. Tiwari, A.S. Chauhan, P.K. Dwivedi, N. Eswara Prasad, Low cost copper zinc tin sulphide (CZTS) solar cells fabricated by sulphurizing sol-gel deposited precursor using 1,2-ethanedithiol (EDT), Sol. Energy vol. 224, (2021) 210–217, https://doi.org/10.1016/j.solener.2021.04.046

[37] M. Courel, M. Picquart, A. Arce-Plaza, F.A. Pulgarin-Agudelo, J.R. González-Castillo, I. Montoya De Los Santos, O. Vigil-Galán, Study on the impact of stoichiometric and optimal compositional ratios on physical properties of Cu_2ZnSnS_4 thin films deposited by spray pyrolysis, Mater. Res. Express vol. 5, (1) (2018) 15513, https://doi.org/10.1088/2053-1591/aaa720

[38] V.S. Zakhvalinskii, T.T.H. Nguyen, T.T. Pham, N.T. Dang, E.A. Piliuk, S.V. Taran, Structural, Optical and Electrical Conductivity Properties of Stannite Cu_2ZnSnS_4, J. Electron. Mater. vol. 46, (6) (2017) 3523–3530, https://doi.org/10.1007/s11664-017-5297-z

[39] V. Najafi, S. Kimiagar, Cd-free Cu_2ZnSnS_4 thin film solar cell on a flexible substrate using nano-crystal ink, Thin Solid Films vol. 657, (2018) 70–75, https://doi.org/10.1016/j.tsf.2018.05.013

[40] J. Henry, K. Mohanraj, G. Sivakumar, Electrical and optical properties of CZTS thin films prepared by SILAR method, J. Asian Ceram. Soc. vol. 4, (1) (2016) 81–84, https://doi.org/10.1016/j.jascer.2015.12.003

[41] S.P. Kandare, S.S. Dahiwale, S.D. Dhole, M.N. Rao, R. Rao, Order-disorder transition in Nano-Cu_2ZnSnS_4: A Raman spectroscopic study, Mater. Sci. Semicond. Process. vol. 102, (2019) 104594, https://doi.org/10.1016/j.mssp.2019.104594

[42] H. Borate, A. Bhorde, A. Waghmare, S. Nair, S. Pandharkar, A. Punde, P. Shinde, P. Vairale, V. Jadkar, R. Waykar, S. Rondiya, Y. Hase, R. Aher, N. Patil, M. Prasad, S. Jadkar, Single-step Electrochemical Deposition of CZTS Thin Films with Enhanced Photoactivity, ES Mater. Manuf. (2020), https://doi.org/10.30919/esmm5f934

[43] B. Ananthoju, J. Mohapatra, M.K. Jangid, D. Bahadur, N.V. Medhekar, M. Aslam, Cation/Anion Substitution in Cu_2ZnSnS_4 for Improved Photovoltaic Performance, Sci. Rep. vol. 6, (1) (2016) 1–11, https://doi.org/10.1038/srep35369

[44] L. Yang, A. Antanovich, A. Prudnikau, O.S. Taniya, K.V. Grzhegorzhevskii, P. Zelenovskiy, T. Terpinskaya, J. Tang, M. Artemyev, Highly luminescent Zn-Cu-In-S/ZnS core/gradient shell quantum dots prepared from indium sulfide by cation exchange for cell labeling and polymer composites, Nanotechnology vol. 30, (39) (2019) 9, https://doi.org/10.1088/1361-6528/ab2aa2

[45] P.S. Maldar, M.A. Gaikwad, A.A. Mane, S.S. Nikam, S.P. Desai, S.D. Giri, A. Sarkar, A.V. Moholkar, Fabrication of Cu_2CoSnS_4 thin films by a facile spray pyrolysis for photovoltaic application, vol. 158, (September) (2017) 89–99, https://doi.org/10.1016/j.solener.2017.09.036

[46] M. Krishnaiah, A. Kumar, J. Song, D. Ph, S.H. Jin, D. Ph, Cu /(Co+Sn) ratio effects on physical and photodetective properties for visible light absorbing Cu_2CoSnS_4 nanoparticles via a one-pot hydrothermal process, J. Alloy. Compd. vol. 847, (2020) 156174, https://doi.org/10.1016/j.jallcom.2020.156174

[47] K.A. Adegoke, M. Iqbal, H. Louis, O.S. Bello, Synthesis, characterization and application of CdS/ZnO nanorod heterostructure for the photodegradation of Rhodamine B dye, Mater. Sci. Energy Technol. vol. 2, (2) (2019) 329–336, https://doi.org/10.1016/j.mset.2019.02.008

[48] K. Pooput, C.H. Lu, W.Y. Shih, W.H. Shih, Stable aqueous wurtzite kesterite suspensions by direct precipitation with capping molecules, J. Nanosci. Nanotechnol. vol. 17, (3) (2017) 2185–2190, https://doi.org/10.1166/jnn.2017.12813

[49] K. Rawat, P.K. Shishodia, Structural and optical properties of sol gel derived Cu_2ZnSnS_4 nanoparticles, Adv. Powder Technol. vol. 28, (2) (2017) 611–617, https://doi.org/10.1016/j.apt.2016.11.013

[50] S. Rondiya, A. Rokade, A. Jadhavar, S. Nair, M. Chaudhari, R. Kulkarni, A. Mayabadi, A. Funde, H. Pathan, S. Jadkar, Effect of calcination temperature on the properties of CZTS absorber layer prepared by RF sputtering for solar cell applications, Mater. Renew. Sustain. Energy vol. 6, (2) (2017) 1–10, https://doi.org/10.1007/s40243-017-0092-6

[51] F. Alirezazadeh, S. Sheibani, Facile mechano-chemical synthesis and enhanced photocatalytic performance of Cu_2ZnSnS_4 nanopowder, Ceram. Int. vol. 46, (17) (2020) 26715–26723, https://doi.org/10.1016/j.ceramint.2020.07.146

[52] E.M. Mkawi, Y. Al-Hadeethi, O. Al-Hartomy, E. Bekyarova, Size-controlling of Cu_2ZnSnS_4 nanoparticles: Effects of stabilizing/reducing agents on material properties, Results Phys. vol. 19, (2020), https://doi.org/10.1016/j.rinp.2020.103407

[53] W. Wang, H. Shen, L.H. Wong, Z. Su, H. Yao, Y. Li, A 4.92% efficiency Cu_2ZnSnS_4 solar cell from nanoparticle ink and molecular solution, RSC Adv. vol. 6, (59) (2016) 54049–54053, https://doi.org/10.1039/c6ra08604g

[54] Y. Hamanaka, W. Oyaizu, M. Kawase, T. Kuzuya, Synthesis of highly non-stoichiometric Cu_2ZnSnS_4 nanoparticles with tunable bandgaps, J. Nanopart. Res. vol. 19, (1) (2017), https://doi.org/10.1007/s11051-016-3704-7

[55] S. Chen, X.G. Gong, A. Walsh, S.H. Wei, Defect physics of the kesterite thin-film solar cell absorber Cu_2ZnSnS_4, Appl. Phys. Lett. vol. 96, (2) (2010) 8–10, https://doi.org/10.1063/1.3275796

[56] D. Lee, K. Yong, Superstrate $CuInS_2$ photovoltaics with enhanced performance using a CdS/ZnO nanorod array, ACS Appl. Mater. Interfaces vol. 4, (12) (2012) 6758–6765, https://doi.org/10.1021/am301957d

[57] M. Zhong, S. Liu, H. Li, C. Li, Superstrate-type Cu_2ZnSnS_4 Solar Cells without Sulfurization Fabricated by Spray Pyrolysis, Chalcogenide Lett. Vol. 15 (3) (2018) 133–137.

[58] A. Ghosh, D.K. Chaudhary, A. Biswas, R. Thangavel, G. Udayabhanu, Solution-processed Cu_2XSnS_4 (X = Fe, Co, Ni) photo-electrochemical and thin film solar cells on vertically grown ZnO nanorod arrays, RSC Adv. vol. 6, (116) (2016) 115204–115212, https://doi.org/10.1039/c6ra24149b

[59] S. Varadharajaperumal, C. Sripan, R. Ganesan, G. Hegde, and M.N. Satyanarayana, "Morphology Controlled n-Type TiO 2 and Stoichiometry Adjusted p-Type Cu2ZnSnS4 Thin Films for Photovoltaic Applications," 2017, doi: 10.1021/acs.cgd.7b00632.

[60] S. Rondiya, N. Wadnerkar, Y. Jadhav, S. Jadkar, S. Haram, M. Kabir, Structural, Electronic, and Optical Properties of Cu_2NiSnS_4: A Combined Experimental and Theoretical Study toward Photovoltaic Applications, Chem. Mater. vol. 29, (7) (2017) 3133–3142, https://doi.org/10.1021/acs.chemmater.7b00149

[61] C. Steinhagen, M.G. Panthani, V. Akhavan, B. Goodfellow, B. Koo, B.A. Korgel, Synthesis of Cu_2ZnSnS_4 Nanocrystals for Use in Low-Cost Photovoltaics. J. Am. Chem. Soc. vol. 131, (35) (2009) 12554–12555 ([Online]. Available), ⟨https://reddog.rmu.edu/login?url=http://search.ebscohost.com/login.aspx?direct=true&db=aph&AN=44475477&site=ehost-live&scope=site⟩.

[62] V.V. Satale, S.V. Bhat, Superstrate type CZTS solar cell with all solution processed functional layers at low temperature, Sol. Energy vol. 208, (2020) 220–226, https://doi.org/10.1016/j.solener.2020.07.055

[63] R. Chen, J. Fan, C. Liu, X. Zhang, Y. Shen, Y. Mai, Solution-processed one-dimensional ZnO@CdS heterojunction toward efficient Cu_2ZnSnS_4 solar cell with inverted structure, Sci. Rep. vol. 6, (October) (2016) 1–9, https://doi.org/10.1038/srep35300